optica

Terahertz hyperspectral imaging with dual chip-scale combs

LUKASZ A. STERCZEWSKI,[1,2,†] JONAS WESTBERG,[1,†] YANG YANG,[3] DAVID BURGHOFF,[3,4] JOHN RENO,[5] QING HU,[3,6] AND GERARD WYSOCKI[1,*]

[1]*Department of Electrical Engineering, Princeton University, Princeton, New Jersey 08544, USA*
[2]*Faculty of Electronics, Wroclaw University of Science and Technology, Wroclaw 50370, Poland*
[3]*Department of Electrical Engineering and Computer Science, Research Laboratory of Electronics, Massachusetts Institute of Technology, Cambridge, Massachusetts 02139, USA*
[4]*Department of Electrical Engineering, University of Notre Dame, Notre Dame, Indiana 46556, USA*
[5]*Center for Integrated Nanotechnology, Sandia National Laboratories, Albuquerque, New Mexico 87123, USA*
[6]*e-mail: qhu@mit.edu*
Corresponding author: gwysocki@princeton.edu

Hyperspectral imaging is a spectroscopic imaging technique that allows for the creation of images with pixels containing information from multiple spectral bands. At terahertz wavelengths, it has emerged as a prominent tool for a number of applications, ranging from nonionizing cancer diagnosis and pharmaceutical characterization to nondestructive artifact testing. Contemporary terahertz imaging systems typically rely on nonlinear optical downconversion of a fiber-based near-infrared femtosecond laser, requiring complex optical systems. Here, we demonstrate hyperspectral imaging with chip-scale frequency combs based on terahertz quantum cascade lasers. The dual combs are free-running and emit coherent terahertz radiation that covers a bandwidth of 220 GHz at 3.4 THz with ~10 μW per line. The combination of the fast acquisition rate of dual-comb spectroscopy with the monolithic design, scalability, and chip-scale size of the combs is highly appealing for future imaging applications in biomedicine and the pharmaceutical industry.

1. INTRODUCTION

Optical imaging techniques have long been indispensable in the natural sciences, with widespread adoption in the fields of biology, astronomy, material science, and medicine. If merged with broadband spectroscopy, the traditional two-dimensional image is expanded into its hyperspectral counterpart, where each pixel represents a spectrum, transforming the image into a three-dimensional hyperspectral data cube. The initial interest in this field was predominantly driven by defense and astronomical applications, but the rapid advances in electronics and computing during recent decades have precipitated widespread adoption of hyperspectral imaging in diverse scientific areas, such as biomedicine, agriculture, and environmental sensing [1–6].

Terahertz (THz) technologies have also experienced a similar growth over the past decades [7–10], propelled in large part by the significant advances in ultrafast lasers and nonlinear optics that have transferred THz generation from bulky gas lasers [11] to more user-friendly fiber-based femtosecond laser systems [12]. For noninvasive imaging [13–15], THz radiation exhibits a number of attractive properties, most notably the ability to propagate through materials that are opaque at higher optical frequencies, including fabrics, papers, and plastics. This property has driven developments in nondestructive quality control and security

imaging to awareness beyond the scientific community. For spectroscopic applications, the excitation of vibrational modes at THz frequencies in many inorganic and organic compounds is highly compelling, not only for chemical identification, but also for discrimination based on the crystal lattice arrangement. In addition, the high sensitivity to water absorption together with the nonionizing property of THz radiation makes this part of the electromagnetic spectrum highly suitable for bioimaging applications, e.g., identification of different types of human tissue based on their water content [16]. Another area of active THz imaging development is the pharmaceutical field, where THz radiation can be used to characterize tablet coating thicknesses [3,4], tablet composition, and degradation of the active ingredients [17].

To date, the most commonly used THz spectroscopy systems are based on interferometric or time-domain sampling techniques, which enable wide spectral coverage with good sensitivities and robust operation, but with significant fundamental limitations. The interferometric Fourier transform spectroscopy (FTS) technique [18], originally developed for the visible and infrared spectral regions, offers unrivaled spectral coverage and ease of use. Unfortunately, THz-FTS suffers from large footprint, low brightness, and slow acquisition as a consequence of using a blackbody radiation source and an optomechanically scanned mirror.

Nevertheless, the broad optical bandwidth and proven reliability of THz-FTS ensures its use in sectors of far-infrared spectroscopy and imaging where ample averaging is permitted.

THz time-domain spectroscopy (THz-TDS) usually relies on electro-optical or photoconductive sampling to reconstruct the electromagnetic field of a THz pulse, where the short pulse durations of modern mode-locked fiber lasers make it inherently broadband with good signal-to-noise ratio (SNR) in the 1–3 THz range. However, just as in FTS systems, the time-domain sampling typically relies on a mechanically scanned optical delay line, which limits the acquisition speed and enlarges the system footprint.

Over the last two decades, a novel approach to reconstructing the optical spectrum of a repetitive pulse train has increasingly gained popularity: the dual-comb spectroscopy (DCS) technique [19,20]. In DCS, a second pulse generator with different repetition rate is used to asynchronously sample the pulse train of the first, a process that results in a time-domain signal in the form of an interferogram, analogous to that obtained in FTS. This scheme eliminates the need for any optomechanical movement, which enables high acquisition speeds (microseconds) and user-friendly operation. Although most of this field primarily involves commercially available fiber-laser-based optical frequency combs (OFCs) operating in the near-infrared, its usefulness has also been demonstrated in both the mid-infrared [21–24] and the THz [25] using nonlinear media for frequency conversion. In 2012, a fundamentally different OFC was demonstrated in the mid-infrared, the quantum cascade laser (QCL) OFC [26], which exploits the nonlinearity of a low-dispersion, electrically pumped, semiconductor gain medium to directly emit comb radiation around an optical frequency defined via careful control of the layered semiconductor growth. This first demonstration was shortly followed by an extension to the THz domain [27], where the intrinsically large device dispersion was compensated by waveguide engineering. Much of the strength of the QCL-OFCs lies in their high optical power per mode, which can reach several milliwatts in the mid-infrared [28] and tens of microwatts in the THz [29], making spectroscopic assessments of highly absorbing media possible. This is especially advantageous when considering spectroscopy of liquids or solids where a trade-off between the

gigahertz-range frequency resolution and the high optical power per mode can be justified. Several examples of chip-scale semiconductor laser-based DCS systems have been demonstrated in the mid-infrared [30–33] and THz [29] with short-term peak SNRs of more than $10^4/\sqrt{s}$ [31,33].

Our proof-of-concept THz hyperspectral imaging system is based on a pair of dispersion-compensated THz-QCL OFCs employed in the asymmetric dual-comb configuration. The system achieves a spectral coverage of ∼220 GHz at a center wavelength of 3.4 THz with more than 10 μW of optical power emitted by each comb. A hyperspectral composite image of a pressed disc consisting of α-D-glucose monohydrate (GMH), α-D-lactose monohydrate (LMH), and L-histidine hydrochloride monohydrate (LHHM) is obtained via a raster scan of the sample. This demonstration of hyperspectral imaging using electrically pumped semiconductor laser frequency combs, fabricated using scalable technology, opens possibilities of future compact hyperspectral imaging systems for applications in biomedicine, biochemistry, and the pharmaceutical industry.

2. EXPERIMENTAL PROCEDURES

The system was designed as shown in Fig. 1(a), where two chip-scale THz-QCL OFCs [see Fig. 1(b)] are arranged to emit antiparallel THz beams that are collimated using a combination of silicon lenses and off-axis parabolic mirrors (see Supplement 1 for more details). The collimated THz light from one of the lasers, the signal OFC, is focused onto the sample. The radiation transmitted through the sample is recollimated and combined with the light emitted from the local oscillator OFC using a silicon beam splitter. The dual-comb light is focused onto a sensitive hot electron bolometer used as a square-law mixer with a 6 dB bandwidth of 5 GHz. Due to the multiheterodyne mixing process of the optical modes from both THz-QCL OFCs, the spectral information from the THz frequency domain is imprinted in the radio-frequency (rf) modulation of the photocurrent, which can be conveniently digitized using an rf spectrum analyzer. The FTS spectra obtained for the two OFCs are shown in Fig. 1(c), where 13 and 16 modes can be observed for the two combs, respectively, resulting in an instantaneous optical coverage of 220 GHz for the DCS
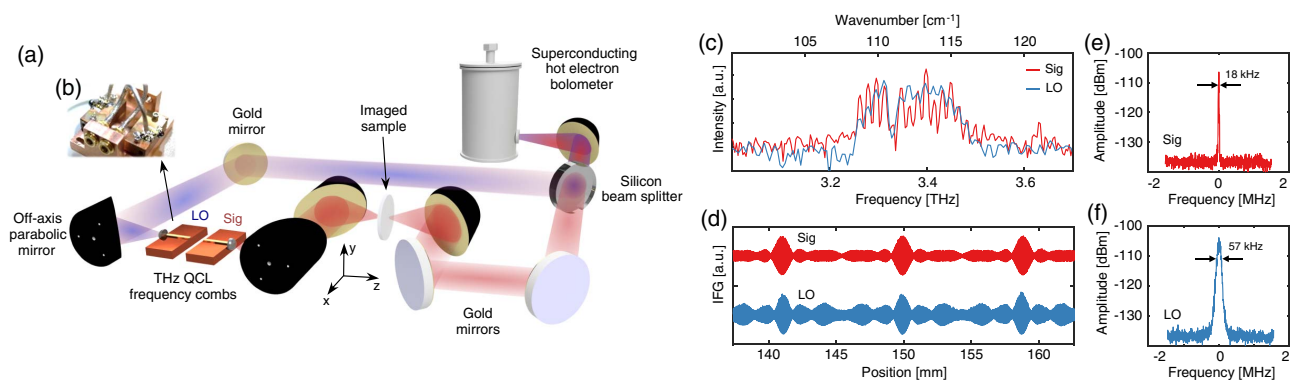
Fig. 1. (a) Dual-comb hyperspectral imaging system. Two THz-QCL OFCs are aligned antiparallel, and their outputs are collected by two off-axis parabolic gold-coated mirrors. The signal OFC is focused on a sample (solid disk) placed on an XYZ translation stage. The transmitted light is collected and combined with the local oscillator comb on a hot electron bolometer with a bandwidth of 5 GHz. (b) Photo of the two chip-scale THz-QCLs mounted on a copper submount; (c) optical mode spectra for the two THz combs centered at around 3.4 THz; (d) interferograms (IFGs) corresponding to the spectra shown in (c), measured with a THz Fourier transform spectrometer (see Supplement 1); (e) and (f) intermode beat notes from the two THz-QCL OFCs. The center frequencies are 16.988 and 17.027 GHz for (e) and (f), respectively.
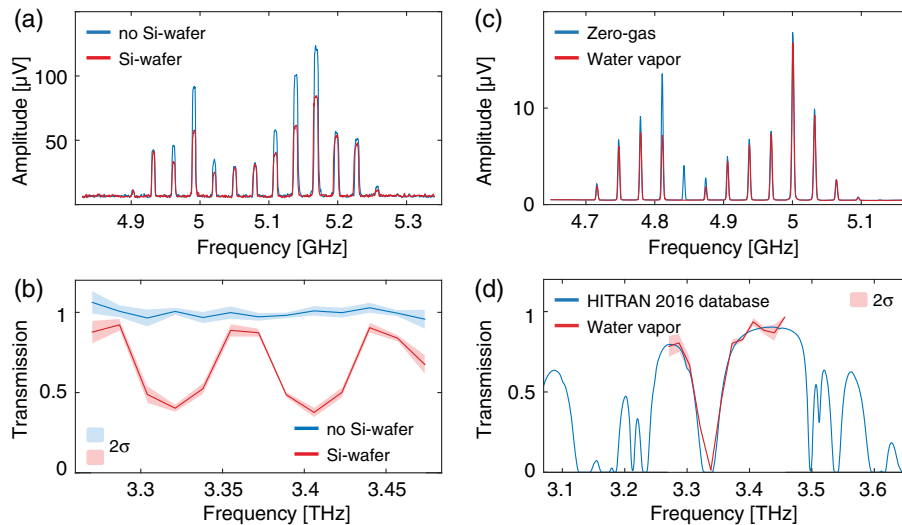
Fig. 2. (a) Beat note spectra acquired for 10 ms with (red) or without (blue) a tilted silicon wafer inserted in the beam path. The beat note amplitude attenuation is clearly observed. (b) Transmission spectra calculated from the beat note spectra in (a). A nearly flat transmission can be observed with a cleared beam path (blue), and the etalon structure originating from the 525 µm Si wafer is shown in red. The shaded areas correspond to a 95% confidence interval. (c) Beat note spectra acquired for 20 ms with zero gas (blue) or atmospheric water vapor at 23% relative humidity (red); (d) transmission spectrum (red) together with a simulation based on parameters from the HITRAN 2016 database [34] (blue). The mode spacings and optical frequencies were determined from Figs. 1(c) and 1(e).

system. Figure 1(d) shows the FTS interferograms for the spectra of Fig. 1(c). Figures 1(e) and 1(f) show narrow and stable rf signals corresponding to the round-trip frequencies measured directly at the OFCs' electrical terminals during operation, which, in combination with broadband FTS spectra, is indicative of comb operation.

3. RESULTS

DCS spectra recorded for a duration of 10 ms are shown in Fig. 2(a), which indicates good signal-to-noise beat notes with an average contrast of more than 20 dB. To estimate the frequency resolution and visualize the behavior of the beat note spectra when the optical modes are affected by optical absorption, a tilted 525 µm silicon wafer is introduced into the beam path, which gives rise to frequency-periodic etalon fringes. The attenuated beat notes are displayed in red. Figure 2(b) shows the corresponding transmission spectra, where the blue trace represents a clear beam path and the red trace the etalon transmission (95% confidence intervals are indicated by the shaded areas). Figures 2(c) and 2(d) show the corresponding measurements for zero-gas and atmospheric water vapor (23% relative humidity) using an acquisition time of 20 ms. These results, together with the spectra of Figs. 1(c) and 1(e), are used for optical frequency calibration of the system.

To evaluate the short-term precision and long-term stability of the system, we performed an Allan deviation analysis [35] of the relative multiheterodyne beat note amplitude stabilities. Rf beat note spectra were recorded with a 100 ms time resolution for a total acquisition time of 500 s. The results are shown in Fig. 3(a), where the shaded area represents the range of precisions observed for all multiheterodyne beat notes. The strongest beat notes with SNRs (1σ) of $\sim 200/\sqrt{s}$ result in proportionally better precisions as compared to the weaker ones with SNRs of $\sim 140/\sqrt{s}$. A drift appears after ~ 20 s of averaging, which is mainly attributed to

mechanical vibrations induced by the cryopump. Figures 3(b) and 3(c) show the histograms of transmission values used for the analysis in Fig. 3(a).

Powdered samples of two common pharmaceutical excipients and an amino acid were pressed to a solid disk in order to demonstrate the hyperspectral imaging capabilities of the system. The disk comprised three zones, with a 10% mass concentration of α-D-GMH, α-D-LMH, and LHHM powder (Sigma-Aldrich,
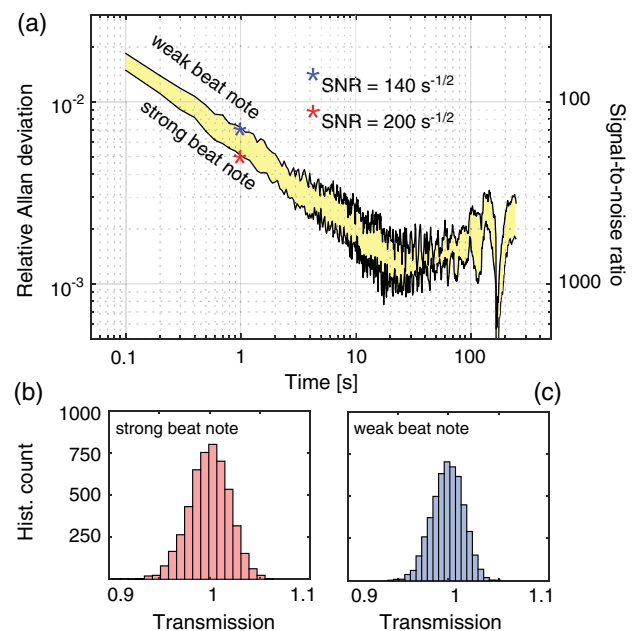
Fig. 3. (a) Allan deviation plot showing the relative stability of the multiheterodyne beat note amplitudes as a function of integration time. The shaded yellow area represents the range of beat note SNRs of the system. (b) and (c) Histograms of transmission values for the strong and weak beat notes of (a).
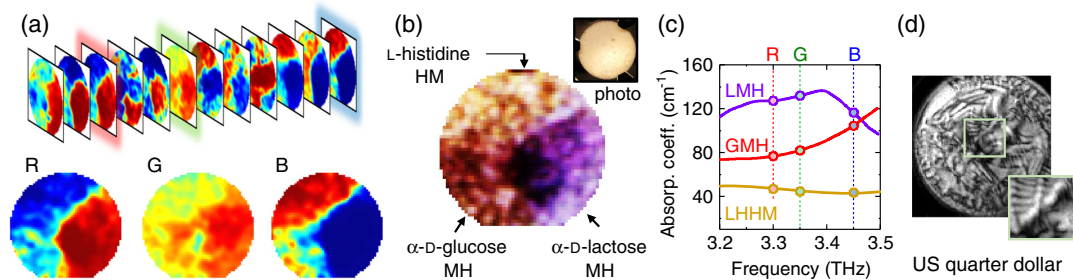
Fig. 4. (a) Individual mean-normalized absorbance hyperspectral slices corresponding to the beat notes shown in Fig. 2(a). False colored R, G, and B show zoomed slices at three selected frequencies: 3.30, 3.35, and 3.45 THz, respectively. The three zones are clearly identifiable. (b) False color RGB composite image composed from slices R, G, and B in transmission mode without mean removal (see Supplement 1). The inset shows a backlit photo of the pressed sample disk. (c) Reference spectroscopic data of α-D-GMH and α-D-LMH from Ref. [36], and LHHM from Ref. [37] showing the frequency-dependent attenuation of the absorbers responsible for the different zone colors in (b); the vertical dashed lines and circles indicate the sampling points of the composite image channels. (d) 111 × 111-pixel reflective intensity imaging of a U.S. quarter to demonstrate the resolution capabilities of the system at this wavelength. The inset shows a finer scan of the details of the eagle's wing.

99%) diluted in spectroscopic grade polyethylene and was pressed using 5 tons of pressure. The disk was placed in a sample holder with XYZ-translation capability, and the sample was raster-scanned across the focus of the THz beam with a step size of 0.5 mm, resulting in a 81 × 53 pixel THz image acquired as a three-dimensional hyperspectral data cube using simultaneously acquired dual-comb spectra. The acquisition time was limited by the movement of the translation stage and the data transfer speed to approximately 0.3 s per pixel, resulting in a total acquisition time of 21 min for the hyperspectral image shown in Fig. 4(b). By upgrading the slow translation stage to faster raster-scan hardware, similar images could potentially be obtained on the subsecond time scale. Simple Gaussian smoothening and contrast enhancing sigmoid transformation was used to obtain the hyperspectral slices shown in Fig. 4(a) (see Supplement 1). Images labeled R, G, and B show selected hyperspectral slices where the different spectral signatures of the material absorption shown in Fig. 4(c) were assigned high-contrast false colors. Two zones stand out due to distinct spectral trends in material absorption, whereas the third zone, as a result of a nearly featureless absorption spectrum in this spectral region, show less contrast. The RGB composite image of Fig. 4(b) is obtained by combining the R, G, and B log-transmission slices (see Supplement 1) of Fig. 4(a), measured at 3.30, 3.35, and 3.45 THz, respectively. The three zones with different compounds are clearly identifiable in the composite image. The bottom-left zone with GMH appears as red in the transmission image due to a monotonically increasing absorption with frequency, as opposed to the bottom-right purple zone of LMH, which has the lowest attenuation in the blue (high-frequency) channel, and the strongest in green. Finally, the top LHHM zone appears as orange-white since it is the most transparent of all, with slightly increased absorption in the blue channel. To demonstrate the resolution capabilities of the system, a reflective intensity image with ~12000 pixels of a U.S. quarter was acquired [see Fig. 4(d)]. The inset shows a finer scan of the details of the feathers on the eagle's wing with <200 μm resolution.

4. CONCLUSION

In conclusion, we have experimentally demonstrated a hyperspectral imaging system using dual chip-scale semiconductor laser frequency combs, all while operating in the challenging THz spectral region. An 81 × 53-pixel hyperspectral image was acquired through a raster scan of a solid pressed disk containing three differently absorbing compounds: α-D-GMH, α-D-LMH, and LHHM. The THz sources operate at a center frequency of 3.4 THz and span approximately 220 GHz with an optical power of ~10 μW per mode, which is more than typically achieved with FTS or time-domain spectroscopy at this wavelength. The acquisition speed of the instrument is currently limited by the slow mechanical raster scan, but assessments of the short-term precision of the system indicate that percentage-level fractional absorption could be obtained on the subsecond time scale with faster scanning.

The ultimate spectral resolution of the system could theoretically reach <100 kHz levels as indicated by the intermode beat note linewidths shown in Figs. 1(e) and 1(f). However, this level of spectral resolution would require intricate frequency stabilization techniques in combination with precise laser frequency control. The nominal spectral resolution of the dual-comb system with free-running lasers is at the megahertz level, given by the linewidth of the multiheterodyne beat notes, but this resolution can only be exploited through step-scan spectral interleaving or continuous frequency tuning. However, in the case of solid samples with broad spectral features, the spectral sampling resolution given by the mode spacing is often sufficient for species identification. Despite the limited spectral coverage (220 GHz) and moderate frequency resolution (~17 GHz), our proof-of-concept system is capable of correctly identifying the tested solids based on their spectral differences in absorbance, but THz frequency comb devices with broader optical coverage are needed for a more quantitative assessment of the samples.

Future developments of the combs are expected to further increase the optical power and address the aforementioned limitations in spectral coverage [38]. Already, octave-spanning multimode THz-QCLs have been demonstrated [39], and continuing efforts to manage the dispersion of these devices are likely to result in similar optical bandwidths for comb operation. In addition, a reduction in the duty cycle of the combs through pulsed operation can be used to increase the operating temperature, albeit with an accompanied loss in sensitivity [29]. Even so, pulsed mode operation of the THz-QCLs combined with multiheterodyne

downconversion via room-temperature Schottky mixers is likely the most viable path towards practical applications, e.g., in bio-imaging or pharmaceutical quality control.

See Supplement 1 for supporting content.

†These authors contributed equally to this work.

REFERENCES

1. A. J. Fitzgerald, V. P. Wallace, M. Jimenez-Linan, L. Bobrow, R. J. Pye, A. D. Purushotham, and D. D. Arnone, "Terahertz pulsed imaging of human breast tumors," Radiology **239**, 533–540 (2006).
2. C. Yu, S. Fan, Y. Sun, and E. Pickwell-MacPherson, "The potential of terahertz imaging for cancer diagnosis: a review of investigations to date," Quant. Imag. Med. Surg. **2**, 33–45 (2012).
3. A. J. Fitzgerald, B. E. Cole, and P. F. Taday, "Nondestructive analysis of tablet coating thicknesses using terahertz pulsed imaging," J. Pharm. Sci. **94**, 177–183 (2005).
4. J. A. Zeitler, Y. Shen, C. Baker, P. F. Taday, M. Pepper, and T. Rades, "Analysis of coating structures and interfaces in solid oral dosage forms by three dimensional terahertz pulsed imaging," J. Pharm. Sci. **96**, 330–340 (2007).
5. E. Abraham, A. Younus, J. C. Delagnes, and P. Mounaix, "Non-invasive investigation of art paintings by terahertz imaging," Appl. Phys. A **100**, 585–590 (2010).
6. J. B. Jackson, M. Mourou, J. F. Whitaker, I. N. Duling, S. L. Williamson, M. Menu, and G. A. Mourou, "Terahertz imaging for non-destructive evaluation of mural paintings," Opt. Commun. **281**, 527–532 (2008).
7. M. Tonouchi, "Cutting-edge terahertz technology," Nat. Photonics **1**, 97–105 (2007).
8. M. A. Belkin, F. Capasso, A. Belyanin, D. L. Sivco, A. Y. Cho, D. C. Oakley, C. J. Vineis, and G. W. Turner, "Terahertz quantum-cascade-laser source based on intracavity difference-frequency generation," Nat. Photonics **1**, 288–292 (2007).
9. B. S. Williams, "Terahertz quantum-cascade lasers," Nat. Photonics **1**, 517–525 (2007).
10. M. S. Vitiello, G. Scalari, B. Williams, and P. D. Natale, "Quantum cascade lasers: 20 years of challenges," Opt. Express **23**, 5167–5182 (2015).
11. S. Jacobsson, "Optically pumped far infrared lasers," Infrared Phys. **29**, 853–874 (1989).
12. B. Sartorius, H. Roehle, H. Künzel, J. Böttcher, M. Schlak, D. Stanze, H. Venghaus, and M. Schell, "All-fiber terahertz time-domain spectrometer operating at 1.5 µm telecom wavelengths," Opt. Express **16**, 9565–9570 (2008).
13. D. M. Mittleman, "Twenty years of terahertz imaging [invited]," Opt. Express **26**, 9417–9431 (2018).
14. A. W. M. Lee, Q. Qin, S. Kumar, B. S. Williams, Q. Hu, and J. L. Reno, "Real-time terahertz imaging over a standoff distance (> 25 meters)," Appl. Phys. Lett. **89**, 141125 (2006).
15. A. W. M. Lee, B. S. Williams, S. Kumar, Q. Hu, and J. L. Reno, "Real-time imaging using a 4.3-THz quantum cascade laser and a 320 × 240 microbolometer focal-plane array," IEEE Photon. Technol. Lett. **18**, 1415–1417 (2006).
16. Q. Sun, Y. He, K. Liu, S. Fan, E. P. J. Parrott, and E. Pickwell-MacPherson, "Recent advances in terahertz technology for biomedical applications," Quant. Imag. Med. Surg. **7**, 345–355 (2017).
17. J. A. Zeitler, D. A. Newnham, P. F. Taday, C. J. Strachan, M. Pepper, K. C. Gordon, and T. Rades, "Temperature dependent terahertz pulsed spectroscopy of carbamazepine," Thermochim. Acta **436**, 71–77 (2005).
18. P. R. Griffiths and J. A. D. Haseth, *Fourier Transform Infrared Spectrometry* (Wiley, 2007).
19. F. Keilmann, C. Gohle, and R. Holzwarth, "Time-domain mid-infrared frequency-comb spectrometer," Opt. Lett. **29**, 1542–1544 (2004).
20. I. Coddington, N. Newbury, and W. Swann, "Dual-comb spectroscopy," Optica **3**, 414–426 (2016).
21. A. V. Muraviev, V. O. Smolski, Z. E. Loparo, and K. L. Vodopyanov, "Massively parallel sensing of trace molecules and their isotopologues with broadband subharmonic mid-infrared frequency combs," Nat. Photonics **12**, 209–214 (2018).
22. G. Ycas, F. R. Giorgetta, E. Baumann, I. Coddington, D. Herman, S. A. Diddams, and N. R. Newbury, "High-coherence mid-infrared dual-comb spectroscopy spanning 2.6 to 5.2 µm," Nat. Photonics **12**, 202–208 (2018).
23. G. Ycas, F. R. Giorgetta, K. C. Cossel, E. M. Waxman, E. Baumann, N. R. Newbury, and I. Coddington, "Mid-infrared dual-comb spectroscopy of volatile organic compounds across long open-air paths," Optica **6**, 165–168 (2019).
24. M. Yu, Y. Okawachi, A. G. Griffith, N. Picqué, M. Lipson, and A. L. Gaeta, "Silicon-chip-based mid-infrared dual-comb spectroscopy," Nat. Commun. **9**, 1869 (2018).
25. T. Yasui, R. Ichikawa, Y.-D. Hsieh, K. Hayashi, H. Cahyadi, F. Hindle, Y. Sakaguchi, T. Iwata, Y. Mizutani, H. Yamamoto, K. Minoshima, and H. Inaba, "Adaptive sampling dual terahertz comb spectroscopy using dual free-running femtosecond lasers," Sci. Rep. **5**, 10786 (2015).
26. A. Hugi, G. Villares, S. Blaser, H. C. Liu, and J. Faist, "Mid-infrared frequency comb based on a quantum cascade laser," Nature **492**, 229–233 (2012).
27. D. Burghoff, T.-Y. Kao, N. Han, C. W. I. Chan, X. Cai, Y. Yang, D. J. Hayton, J.-R. Gao, J. L. Reno, and Q. Hu, "Terahertz laser frequency combs," Nat. Photonics **8**, 462–467 (2014).
28. P. Jouy, J. M. Wolf, Y. Bidaux, P. Allmendinger, M. Mangold, M. Beck, and J. Faist, "Dual comb operation of λ–8.2 µm quantum cascade laser frequency comb with 1 W optical power," Appl. Phys. Lett. **111**, 141102 (2017).
29. Y. Yang, D. Burghoff, D. J. Hayton, J.-R. Gao, J. L. Reno, and Q. Hu, "Terahertz multiheterodyne spectroscopy using laser frequency combs," Optica **3**, 499–502 (2016).
30. G. Villares, A. Hugi, S. Blaser, and J. Faist, "Dual-comb spectroscopy based on quantum-cascade-laser frequency combs," Nat. Commun. **5**, 5192 (2014).
31. J. Westberg, L. A. Sterczewski, and G. Wysocki, "Mid-infrared multiheterodyne spectroscopy with phase-locked quantum cascade lasers," Appl. Phys. Lett. **110**, 141108 (2017).
32. L. A. Sterczewski, J. Westberg, C. L. Patrick, C. S. Kim, M. Kim, C. L. Canedy, W. W. Bewley, C. D. Merritt, I. Vurgaftman, J. R. Meyer, and G. Wysocki, "Multiheterodyne spectroscopy using interband cascade lasers," Opt. Eng. **57**, 011014 (2017).
33. J. L. Klocke, M. Mangold, P. Allmendinger, A. Hugi, M. Geiser, P. Jouy, J. Faist, and T. Kottke, "Single-shot submicrosecond mid-infrared spectroscopy on protein reactions with quantum cascade laser frequency combs," Anal. Chem. **90**, 10494–10500 (2018).
34. I. E. Gordon, L. S. Rothman, C. Hill, R. V. Kochanov, Y. Tan, P. F. Bernath, M. Birk, V. Boudon, A. Campargue, K. V. Chance, B. J. Drouin, J. M. Flaud, R. R. Gamache, J. T. Hodges, D. Jacquemart, V. I. Perevalov, A. Perrin, K.

P. Shine, M. A. H. Smith, J. Tennyson, G. C. Toon, H. Tran, V. G. Tyuterev, A. Barbe, A. G. Császár, V. M. Devi, T. Furtenbacher, J. J. Harrison, J. M. Hartmann, A. Jolly, T. J. Johnson, T. Karman, I. Kleiner, A. A. Kyuberis, J. Loos, O. M. Lyulin, S. T. Massie, S. N. Mikhailenko, N. Moazzen-Ahmadi, H. S. P. Müller, O. V. Naumenko, A. V. Nikitin, O. L. Polyansky, M. Rey, M. Rotger, S. W. Sharpe, K. Sung, E. Starikova, S. A. Tashkun, J. V. Auwera, G. Wagner, J. Wilzewski, P. Wcisło, S. Yu, and E. J. Zak, "The HITRAN2016 molecular spectroscopic database," J. Quant. Spectrosc. Radiat. Transfer **203**, 3–69 (2017).

35. P. Werle, R. Mücke, and F. Slemr, "The limits of signal averaging in atmospheric trace-gas monitoring by tunable diode-laser absorption spectroscopy (TDLAS)," Appl. Phys. B **57**, 131–139 (1993).

36. P. Dean, N. K. Saat, S. P. Khanna, M. Salih, A. Burnett, J. Cunningham, E. H. Linfield, and A. G. Davies, "Dual-frequency imaging using an electrically tunable terahertz quantum cascade laser," Opt. Express **17**, 20631–20641 (2009).

37. S. Zong, G. Ren, S. Li, B. Zhang, J. Zhang, W. Qi, J. Han, and H. Zhao, "Terahertz time-domain spectroscopy of L-histidine hydrochloride monohydrate," J. Mol. Struct. **1157**, 486–491 (2018).

38. Y. Yang, A. Paulsen, D. Burghoff, J. L. Reno, and Q. Hu, "Lateral heterogeneous integration of quantum cascade lasers," ACS Photon. **5**, 2742–2747 (2018).

39. M. Rösch, G. Scalari, M. Beck, and J. Faist, "Octave-spanning semiconductor laser," Nat. Photonics **9**, 42–47 (2014).